Soil Dynamics and Earthquake Engineering 136 (2020) 106196

Contents lists available at ScienceDirect

Soil Dynamics and Earthquake Engineering

journal homepage: http://www.elsevier.com/locate/soildyn

Coupling of SPT and 3D full waveform inversion for deep site characterization

Majid Mirzanejad [a], Khiem T. Tran [a,*], Michael McVay [a], David Horhota [b], Scott J. Wasman [a]

[a] University of Florida, Department of Civil and Coastal Engineering, 365 Weil Hall, P.O. Box 116580, Gainesville, FL, 32611, USA
[b] Florida Department of Transportation, 5007 N.E. 39th Avenue Gainesville, FL, 32609, USA

ARTICLE INFO

Keywords:
SPT
3D waveform inversion
Deep foundation
Site characterization

ABSTRACT

Detailed information of soil/rock variability and properties for the entire volume of supporting materials is crucial for the successful design and construction of deep foundations. Traditional invasive testing methods such as the standard penetration test (SPT) and the cone penetrometer test (CPT) only sample a small volume of soil/rock properties near the device's tip. Surface-based seismic methods can provide overall subsurface conditions but are limited to shallow depths due to the dominancy of surface waves. To address this issue, we present a novel SPT-seismic testing method for deep site characterization. Seismic wavefields generated by SPT blows at various depths are recorded by a 2D grid of geophones on the ground surface, and analyzed by a 3D full-waveform inversion (3D FWI) to extract subsurface material properties. Unlike surface-based wavefields dominated by surface waves propagating near the ground surface, the SPT-seismic wavefields are rich in body waves propagating from great depths that allow extracting detailed material properties at depths. The method is tested on in-depth source synthetic data and SPT-source field data. The results of the synthetic experiment indicate that the method successfully images soil layering with a buried anomaly. Field experiment results provide new insights into its utility as a viable geophysical tool for deep site characterization. 3D subsurface S-wave and P-wave velocities within 9 m around the SPT boring are well characterized, including two deep voids at 14–18 m depth. Comparison with the surface-based 3D FWI method proves the superiority of the presented method in imaging deep structures. S-wave velocity values of the final inverted result are also compared with SPT N-values and a good overall agreement over the whole depth is observed.

1. Introduction

Foundations beneath any structure may exist near the surface (i.e. shallow foundation) to over 50 m (e.g. deep foundation) depending on the magnitude of the loads and soil/rock conditions at the site. For instance, with limited right of way, large loads, vibration concerns, high water and loose sand over rock, drilled shafts or auger cast piles may be the foundation of choice. One of the challenges in the design and construction of deep foundations is the lack of certainty in the underlying soil/rock conditions. Traditional invasive testing methods such as SPT and CPT are regularly used as part of the geotechnical site investigation. In the case of weathered or competent rock, SPT and core drilling are employed. However, they are very limited in quantity of material tested compared to size of foundation elements within a pile cap or bent.

Surface-based geophysical tests can provide overall subsurface conditions and are a good supplement to the invasive methods. For example, 3D seismic waveform tomography methods [1–3] can be a powerful tool in visualizing subsurface features. However, detection of voids buried in bedrock with surface-based methods is limited by the void size and location, since only a small portion of the surface energy passes into the rock.

Crosshole and downhole seismic methods are commonly used in exploration geophysics and mining industry to characterize properties of the subsurface soil and rock [4,5]. They rely on placing either the source or receiver in the ground using a single (downhole) or multiple (crosshole) boreholes. This allows for the utilization of transmission/diffraction data as compared to only reflection/refraction data commonly encountered in surface-based surveys. Taking both the source and receiver array below the ground surface can also reduce high frequency attenuations allowing smaller earth structures to be

---

* Corresponding author.

E-mail addresses: m.mirzanejad@ufl.edu (M. Mirzanejad), ttk@ufl.edu (K.T. Tran), mcm@ce.ufl.edu (M. McVay), david.horhota@dot.state.fl.us (D. Horhota), scott.wasman@essie.ufl.edu (S.J. Wasman).

https://doi.org/10.1016/j.soildyn.2020.106196
Received 26 November 2019; Received in revised form 5 February 2020; Accepted 24 April 2020

characterized [6].

Several studies have investigated different aspects of modelling and analyzing crosshole seismic data using tomographic methods [6–16]. The crosshole methods can provide the detailed properties of materials between boreholes. However, they require at least two boreholes. Alternatively, Tran and Hiltunen [17], combined surface and borehole data for 2D tomography to a single borehole to reduce cost.

In this study, we present a new SPT-seismic testing method, which is a combination of SPT and 3D full-waveform inversion (3D FWI) to improve characterized resolution and accuracy with depths. Since SPT testing in weathered and karst rock is the standard practice, its use as an energy source for geophysical investigation is of great interest. Specifically, as the drill rod and sampler within the rock is struck with SPT hammer (N-values), seismic wavefields are generated and recorded with a grid of geophones on the ground surface. Unlike surface-based sources that generate predominately surface waves, the SPT-seismic device generates body waves that originate wherever the SPT sampler is located. Moreover, analyses of the body waves (transmission/diffraction data) generated from a point source within the rock mass that arrives at the ground surface will provide higher characterized resolution (i.e. outside of borehole) at much greater depths (i.e. SPT borehole depths) compared to surface-based methods. It is also more cost effective than existing crosshole methods and can be readily applied whenever an SPT test is used.

To assess the potential of SPT-seismic testing, the recently developed 3D elastic full-waveform inversion technique based on the Gauss-Newton approach (3D GN-FWI) reported by Ref. [2] was used to investigate the approach. The analysis started with data generated from a challenging synthetic experiment. It was then tested on SPT-source field data, and the generated geophysical properties were subsequently compared with recorded SPT N-values. The same synthetic and field experiments were also run on the surface-based energy source and compared with the in-depth/SPT-source data. Testing methodology, interpretation and visualization of the inverted results are discussed in the following sections.

2. Methodology and implementation

The 3D GN-FWI method used in this study was recently reported in detail by Ref. [2]; and is briefly summarized in the two steps shown below:

1) A forward 3D elastic wave propagation described by the following stress equilibrium and constitutive equations is performed:

$$\rho\frac{\partial v_i}{\partial t}=\frac{\partial \sigma_{ij}}{\partial x_j}+f_i \tag{1}$$

$$\frac{\partial \sigma_{ij}}{\partial t}=\lambda\frac{\partial v_k}{\partial x_k}+2\mu\frac{\partial v_i}{\partial x_j} \quad \mathit{if} \quad i=j \tag{2}$$

$$\frac{\partial \sigma_{ij}}{\partial t}=\mu\left(\frac{\partial v_i}{\partial x_j}+\frac{\partial v_j}{\partial x_i}\right) \quad \mathit{if} \quad i\neq j \tag{3}$$

In the above equations, σ_{ij} is the ij-th stress component (i, j = 1, 2, 3), v_i is the particle velocity, f_i is the external body force, ρ is the mass density, and λ and μ are Lamé's coefficients. Repetition of a subscript (e.g. k, k) denotes summing over the indices (k = 1, 2, 3).

The finite-difference method with staggered-grids [18] is used to solve the wave equations. The image technique [19] is used to simulate the free-surface boundary condition at the ground surface (top), and the perfectly matched layer (PML) [20] is used at the remaining boundaries (side and bottom) to eliminate spurious reflection back into the model domain. See Ref. [1] for detail on the forward simulation.

2) Then, the Gauss-Newton optimization is iteratively used to minimize the error between the simulated and measured data to extract individual cell material properties. The mathematical formalism of the Gauss-Newton method is given as:

$$\boldsymbol{\Delta d}_{s,r}=\boldsymbol{F}_{s,r}(\boldsymbol{m}) \quad \boldsymbol{d}_{s,r} \tag{4}$$

$$E(\boldsymbol{m})=\frac{1}{2}\boldsymbol{\Delta d}^2=\frac{1}{2}\boldsymbol{\Delta d}^{\mathrm{t}}\boldsymbol{\Delta d}, \mathit{and}\ \boldsymbol{\Delta d}=\left\{\boldsymbol{\Delta d}_{s,r}, s=1...Ns, r=1...Nr\right\} \tag{5}$$

$$\boldsymbol{m}^{n+1}=\boldsymbol{m}^{n} \quad \alpha^n[\boldsymbol{J}^{\mathrm{t}}\boldsymbol{J}+\lambda_1\boldsymbol{P}^{\mathrm{t}}\boldsymbol{P}+\lambda_2\boldsymbol{I}^{\mathrm{t}}\boldsymbol{I}]\ ^{1}\boldsymbol{J}^{\mathrm{t}}\boldsymbol{\Delta d} \tag{6}$$

$$\boldsymbol{J}^{p}_{s,r}=\frac{\partial \boldsymbol{F}_{s,r}(\boldsymbol{m})}{\partial m_p}=\frac{\boldsymbol{F}_{s,r}\left(\boldsymbol{m}+\Delta m_p\right) \quad \boldsymbol{F}_{s,r}(\boldsymbol{m})}{\Delta m_p} \tag{7}$$

Equation (4) calculates the waveform residual, which is minimized to obtain material parameters (e.g. Vs and Vp). In this equation, $\boldsymbol{F}_{s,r}(m)$ denotes the simulated data (solution of equations (1)–(3)) for model **m**. The indices s and r denote the s-th shot and r-th receiver, respectively. Model **m** consists of Vs and Vp of cells and is stored in a column vector. Similarly, $\boldsymbol{d}_{s,r}$ denotes the observed data gathered from the field experiment, and is stored in a column vector. Equation (5) is the L2-norm misfit belonging to the current model **m**. The transcript t denotes the transpose, and Ns and Nr are the number of shots and receivers, respectively.

Equation (6) is the crux of the presented Gauss-Newton implementation and denotes the model update. The current model $\mathbf{m}^{\mathbf{n}}$ is updated to $\mathbf{m}^{\mathbf{n+1}}$ and is used in the next forward iteration. **J** is the Jacobian matrix, which denotes the derivative wavefield. Symbol **I** stands for the identity matrix and **P** is a matrix representing a 3D Laplacian operator. Parameter α^n denotes the step length, which is fixed at 0.5 for the whole analysis. Parameters λ_1 and λ_2 are used to improve the invertibility of the approximate Hessian matrix ($\boldsymbol{H}_a=\boldsymbol{J}^t\boldsymbol{J}$) and regularization. Values λ_1 and λ_2 can range from zero to infinity, with larger values leading to more optimization stability but results in smoother inverted models. Using trial runs, coefficients λ_1 and λ_2 of 0.02 and 0.0005 times of the maximum value of $\boldsymbol{J}^t\boldsymbol{J}$ respectively were found to give a good compromise.

Equation (7) is the formal definition of the Jacobian (**J**) and denotes the derivative wavefield with respect to each model parameter (m_p). By perturbing each parameter, the explicit calculation of Jacobian **J** using equation (7) requires a total of $Ns\ \times\ (M+1)$ forward simulations, with M being the number of parameters (unknowns). Obviously, it is too computationally intensive for 3D problems with tens of thousands of unknowns. To make the calculation more efficient, an implicit method was developed by Ref. [[2]] as:

$$\boldsymbol{J}^{p}_{s,r}=\boldsymbol{F}_x{*}\boldsymbol{R}_x+\boldsymbol{F}_y{*}\boldsymbol{R}_y+\boldsymbol{F}_z{*}\boldsymbol{R}_z \tag{8}$$

where $\boldsymbol{F_x}$, $\boldsymbol{F_y}$ and $\boldsymbol{F_z}$ are the virtual sources in x, y and z directions, computed from the forward wavefields (see Eqs (9)-(14) of [2] for the governing equations). $\boldsymbol{R_x}$, $\boldsymbol{R_y}$ and $\boldsymbol{R_z}$ are the backward wavefields in x, y and z directions. The forward and backward wavefields are simulated by applying an active source at the s-th shot and r-th receiver locations, respectively. The symbol * denotes the convolution operator. Using equation (8), only (Ns + Nr) forward simulations are required to calculate **J**. Finally, a bold character represents either a vector or matrix of component terms.

3. Synthetic experiment

3.1. In-depth source data

To test the feasibility of the SPT-seismic approach, a synthetic simulation was performed prior to a field experiment. The geometry and test configuration of the simulation and field experiment were similar: a 2D array of 6 × 6 receivers at 3 m spacing placed on the ground surface, and a linear array of 35 sources at 0.6 m spacing placed along a vertical line at the center (Fig. 1a). A medium of 20.4 × 18 × 18 m (depth ×

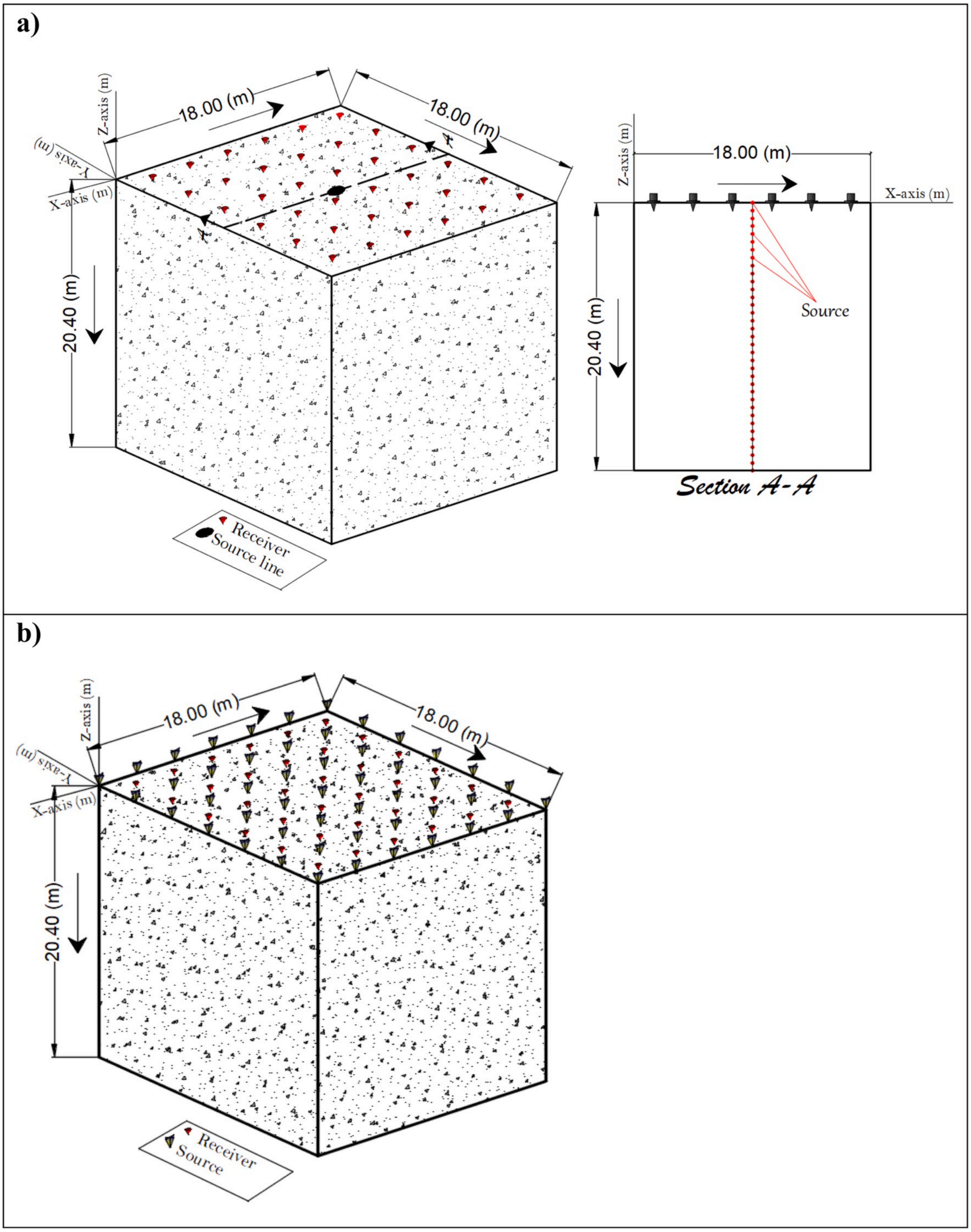

Fig. 1. Synthetic test configuration of the in-depth source geometry (a), and surface-based geometry (b).

length × width) with a grid spacing of 0.6 × 0.75 × 0.75 m (depth × length × width) was used for the analysis. The grid spacing was chosen to facilitate source and receiver placement in the numerical grid. A smaller grid spacing was used with depth to provide more flexibility when assigning actual SPT-source locations.

For the synthetic experiment, a challenging velocity model representing a variable subsurface profile with Vs of 200 m/s for the top layer and 400 m/s for the lower half space, with twice Vs for the Vp profile was used as the true model (Fig. 2a). Furthermore, a buried void of 3 × 3.75 × 3.75 m (depth × length × width) was placed at 15 m depth and 1.0 m away from the source line (or SPT borehole location). It was placed to simulate a deep void that would not be found with the single SPT borehole. The void was assumed to be filled with air with Vs of 0 m/s and Vp of 300 m/s. A mass density of 1800 kg/m^3 is assumed for the whole medium, as a typical value for general soils. The true model was then used as the input in the elastic forward solver based on Eqs (1)–(3) to generate waveform data, using the in-depth source configuration shown in Fig. 1a. Ricker wavelet source signals of the central frequencies of 20 Hz and 30 Hz were then used in the forward simulation to generate two waveform datasets. The generated datasets were then treated as if they came from a field experiment and analyzed by the 3D GN-FWI. This known velocity profile provides a benchmark to compare with the

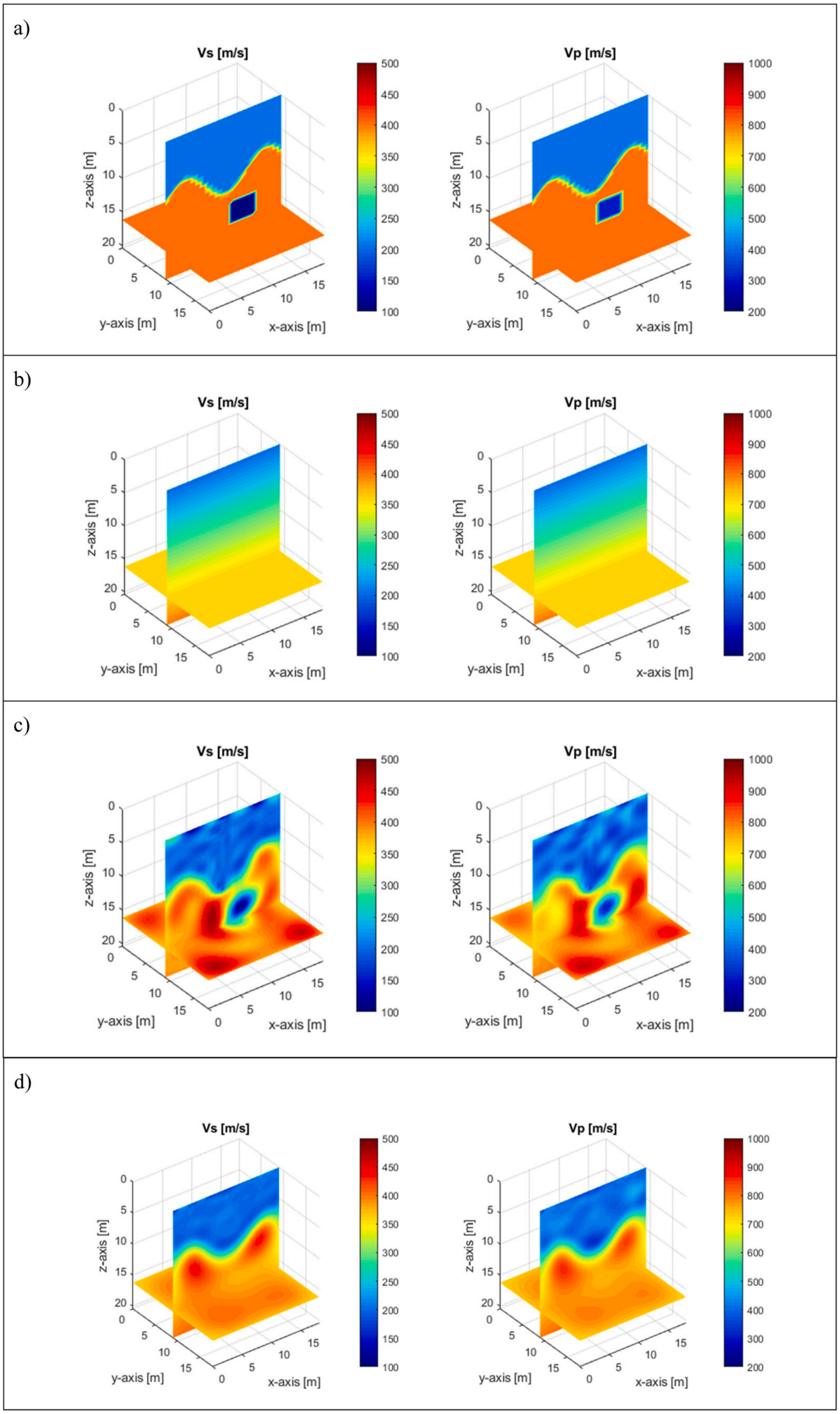

Fig. 2. Synthetic experiment: velocity distribution of Vs and Vp (m/s) for the true model (a), initial model (b) and the final inverted results for the in-depth source data (c) and the surface-based data (d).

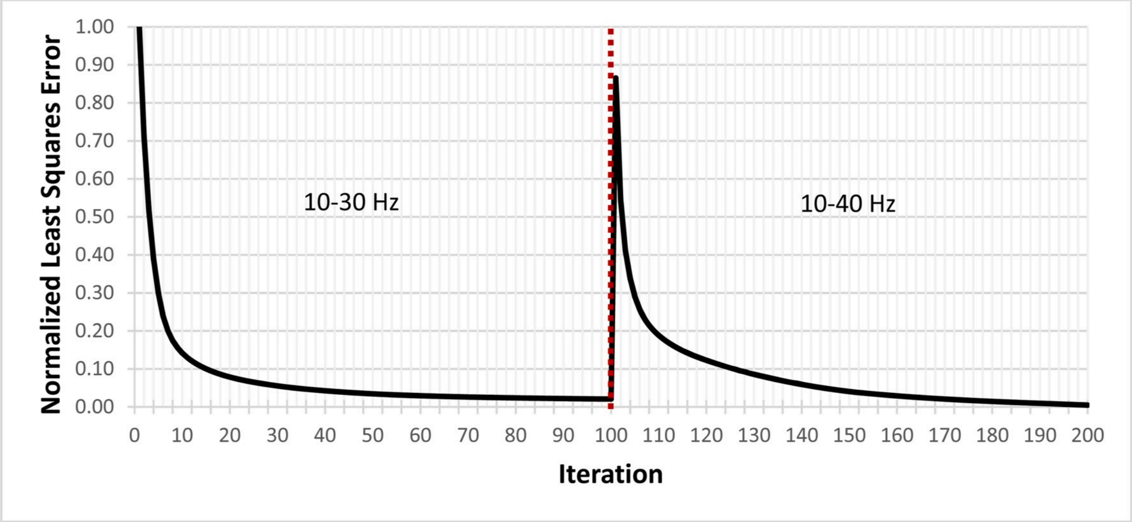

Fig. 3. Synthetic experiment: normalized least squares error for the synthetic experiment with the in-depth source.

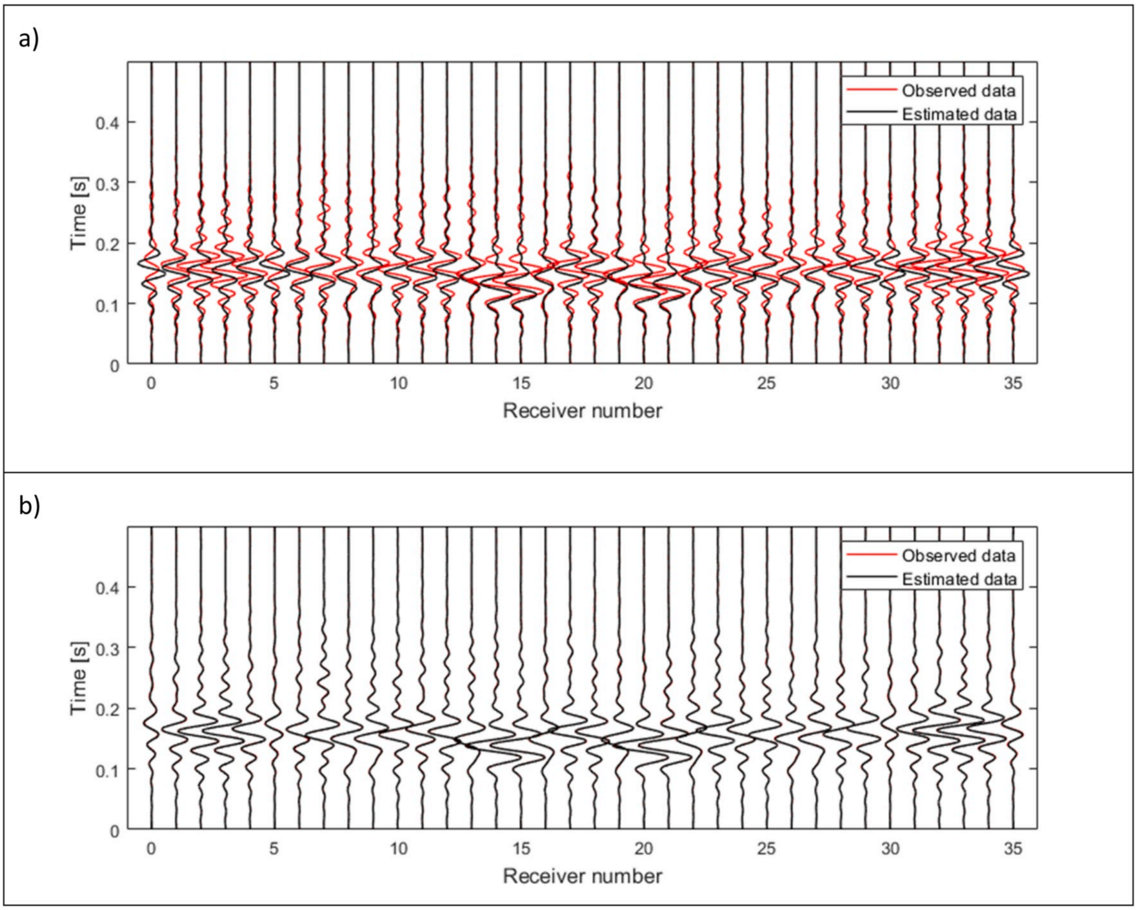

Fig. 4. Synthetic experiment: waveform comparison for a sample shot between the observed data from the true model and estimated data associated with a) the initial model and b) the final inverted result at iteration 200.

inverted results and identifies the expected resolution of the actual field experiment.

A linearly increasing velocity model of 200 m/s at the ground surface to 400 m/s at the half space for the Vs and twice of that for the Vp was used as the initial model (Fig. 2b). This initial model can be obtained from a spectral analysis of measured data as discussed in the field experiment later. Two inversions were conducted in the order of increasing frequency data. The first inversion began with the initial model (Fig. 2b), using the 20 Hz source dataset filtered through 10–30 Hz bandpass algorithm. The second inversion ran with the 30 Hz source data filtered through 10–40 Hz bandpass, using the result of the first inversion as the input velocity model. Both inversions ran for a preset number of iterations (100) and took a total of about 30 h on a workstation computer with 36 cores of 3.2 GHz, and 300 GB of RAM.

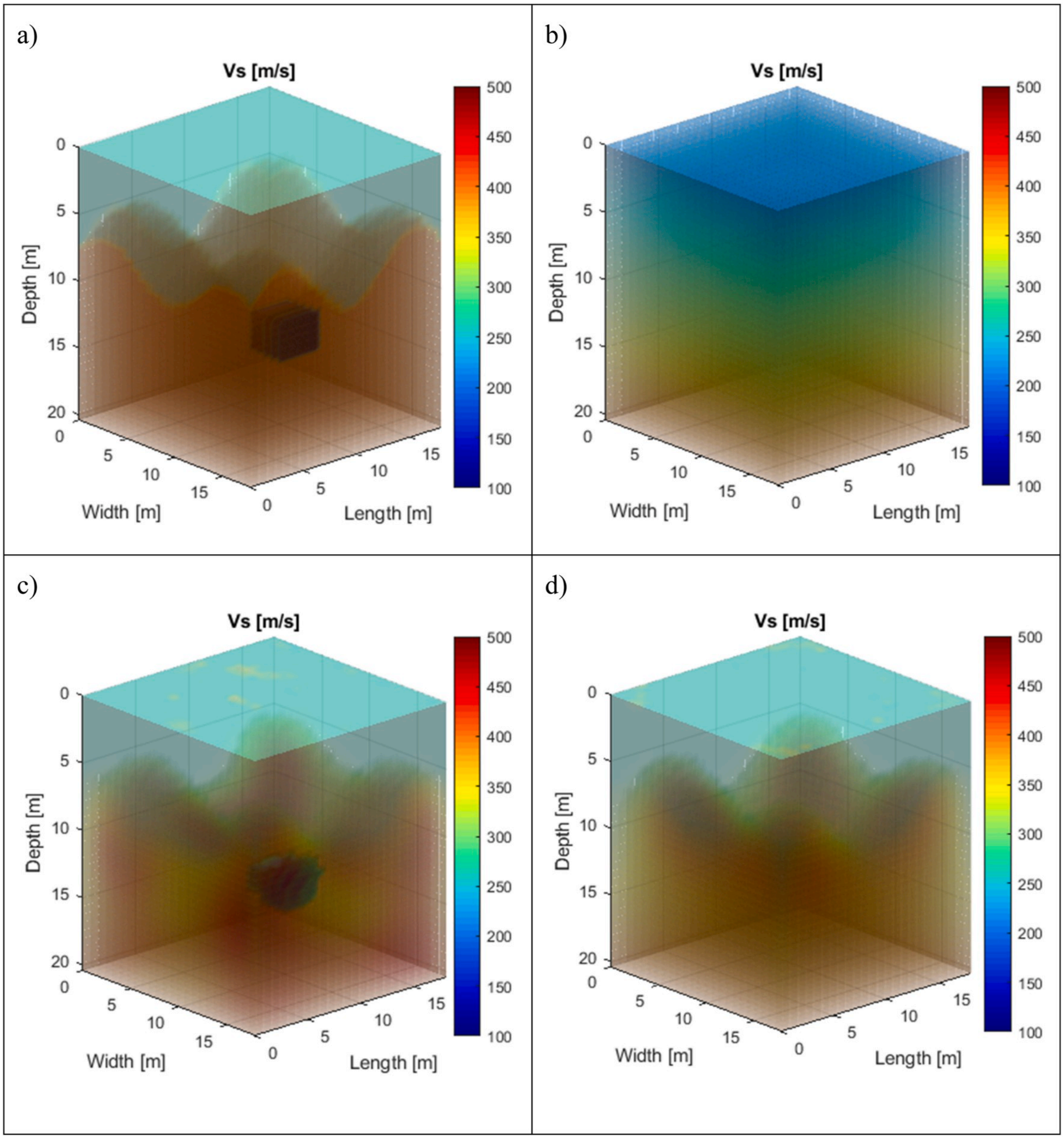

Fig. 5. Synthetic experiment: 3D rendering of the true model using Vs (m/s) (a), initial model (b), the inverted results of the in-depth source (c) and surface-based data (d).

Shown in Fig. 3 is the variation of the normalized least squares error with iterations for both stages of frequency inversion. The error decreased continuously during the first stage from 1.0 at the start of the 10–30 Hz frequency stage to about 0.01 at the end of 100 iterations. Adding the second stage high frequency data of 10–40 Hz created a sharp increase in the least square error. This is due to the velocity profile was not yet ready to propagate the higher frequency data, and hence produced large mismatch in the waveforms. The inversion algorithm was subsequently able to reduce the mismatch and reduced the error to less than 0.01 at the end of the second stage - additional 100 iterations. Shown in Fig. 4 is the waveform comparison between the observed data from the true model and estimated data associated with the initial model (Fig. 4a) and the final inverted model at iteration 200 (Fig. 4b). The waveform match improved substantially during inversion. Phase and amplitudes are matched perfectly at the end, indicating the success of the inversion algorithm that vectored towards the global minimum.

Shown in Fig. 2c is the final inverted result for the in-depth source data. Both Vs and Vp profiles are well characterized. The existence of two separate layers is clearly observed, and the variable layer interface is well imaged. More importantly, the location and overall shape of the deep void is successfully identified. This synthetic result shows a great potential of using the in-depth source data (e.g. generated by a SPT-drill rod and spoon) for characterization of materials around the SPT boring and offline anomalies/voids.

3.2. Surface-based data

To assess the superiority of the in-depth SPT source approach, a 3D FWI analysis of surface-based data was also conducted. The surface-based data were generated on the same true model (Fig. 2a). Both sources and receivers were however located on the free surface, in 2D uniform grids of 7 × 7 and 6 × 6, respectively, at 3 m spacing (Fig. 1b). The surface-based data were analyzed by the 3D GN FWI in the same manner as the in-depth source data. Again, two inversions were conducted for the data at two frequency bandwidths of 10–30 Hz and 10–40 Hz, using the same initial model (Fig. 2b). Both inversions stopped at

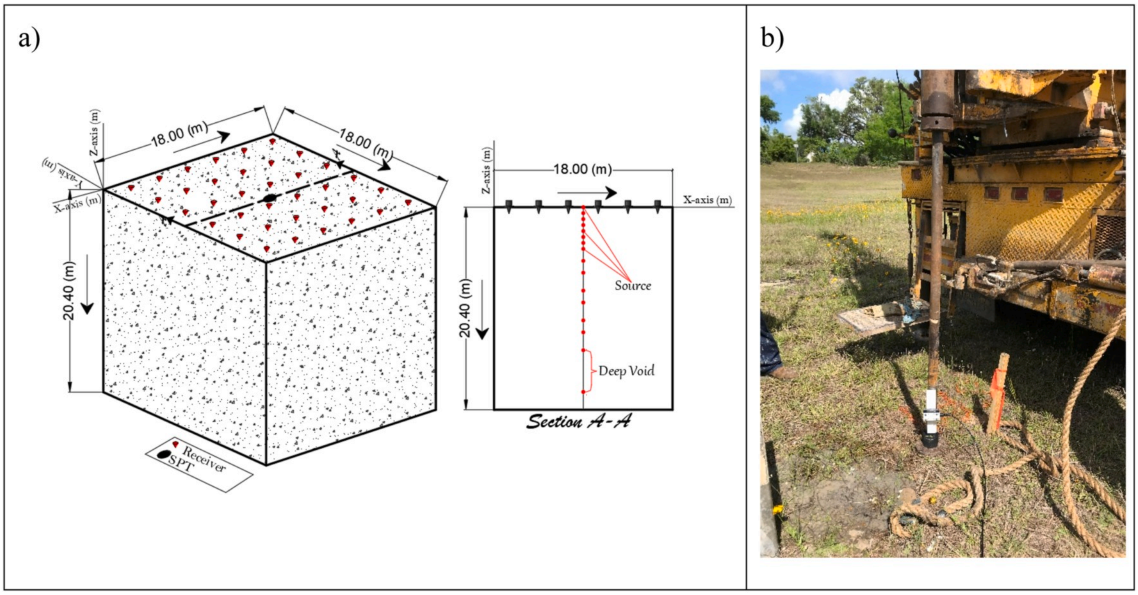

Fig. 6. Field test configuration (a) and SPT rig testing pictures (b). The SPT-source locations are not uniform (different to the synthetic experiment shown in Fig. 1), as the source locations are controlled by the advancement of SPT spoon during field experiment.

100 iterations and took a total of about 38 h on the same workstation computer.

Shown in Fig. 2d is the final inverted result for the surface-based data. The two layers and the layer interface are well imaged. However, there is no indication of the void in the inverted result. This suggests that the surface-based data did not contain enough information of the void in the recorded waveforms. This is due to the deep void being buried at 15 m depth (4 void diameters) with limited test area on the surface (18 by 18 m). The large reflections at the layer boundary of high velocity contrast (i.e. larger impedance) as well as dominated Rayleigh waves in the surface-based data overwhelmed reflections (if any) from the void. The comparison of inverted results in Fig. 2c and d clearly shows the superiority of the in-depth source data in recovering the deep void.

For better viewing, shown in Fig. 5a to d are 3D renderings of the true model, the initial model, the inverted result of the in-depth source data, and the inverted result of the surface-based data, respectively. These renderings are created by passing 2D transects through all the grid points and setting the transparency level to the various velocity scales. This allows for a quick inspection of the entire model space and is a good indicator of the performance of the 3D GN-FWI method. Again, both test methods successfully characterized the layer interface. However, the surface-based method failed to identify the existence of the void. On the other hand, the in-depth source method has successfully identified the void and characterized its position and overall shape.

4. Field experiment

The in-depth SPT source waveform method was subsequently tested with field data gathered at a site in Newberry, Florida. For the field experiment, 36 4.5-Hz vertical geophones covering a 6 × 6 grid of 3 m spacing were placed on the ground surface (Fig. 6a). The Florida Department of Transportation (FDOT) State Material Office's CME 75 SPT rig was used for the in-depth seismic source. An automatic SPT hammer, 63.5 kg (140 lb) was dropped from a height of 760 mm (30 inch) to generate seismic wavefields at each source location with depth (Fig. 6b). To record the seismic data, a seismic trigger was mounted on the SPT rod to activate the seismograph. Seismic wavefields from 16 SPT blows were recorded, together with the 16 depths of the SPT spoon as source locations (Fig. 6a). As the source locations were dictated by the advancement of the SPT spoon, they are not located uniformly with depth.

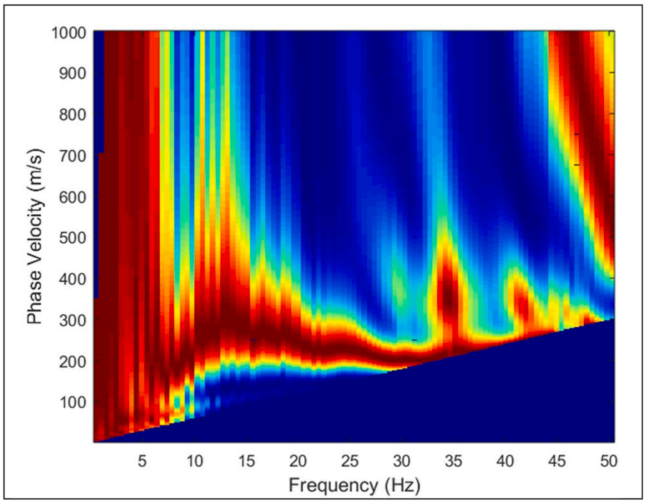

Fig. 7. Spectral analysis of the surface field data of one line of receivers.

In addition, for comparison purpose, standard surface-based testing was also conducted with 49 source locations covering a 7 × 7 grid at 3 m spacing on the ground surface, like that of the synthetic experiment (Fig. 1b). A propelled energy generator with 40 kg dropped weight (PEG, 40 kg) was used as the source of the seismic waves on the ground surface. The same 36 geophones on the 6 × 6 grid of 3 m spacing were used to record surface-based data.

To get a suitable initial model for waveform analysis, a spectral analysis of surface waves was performed using a line of six geophones on the ground surface (Fig. 7). The results suggested a Rayleigh wave velocity of about 200–350 at the frequency spectrum of 10–30 Hz. A linearly increasing initial velocity model was developed with Vs of 200 m/s at the surface to 350 m/s for the underlying half space of the analyzed medium (Fig. 8a left). Vp was determined from Vs and an assumed Poisson's ratio of 0.3 to be almost two times that of Vs (Fig. 8a right). A mass density of 1800 kg/m^3 was assumed as the characteristic density for general soil/rock and was kept constant throughout the analysis. It is

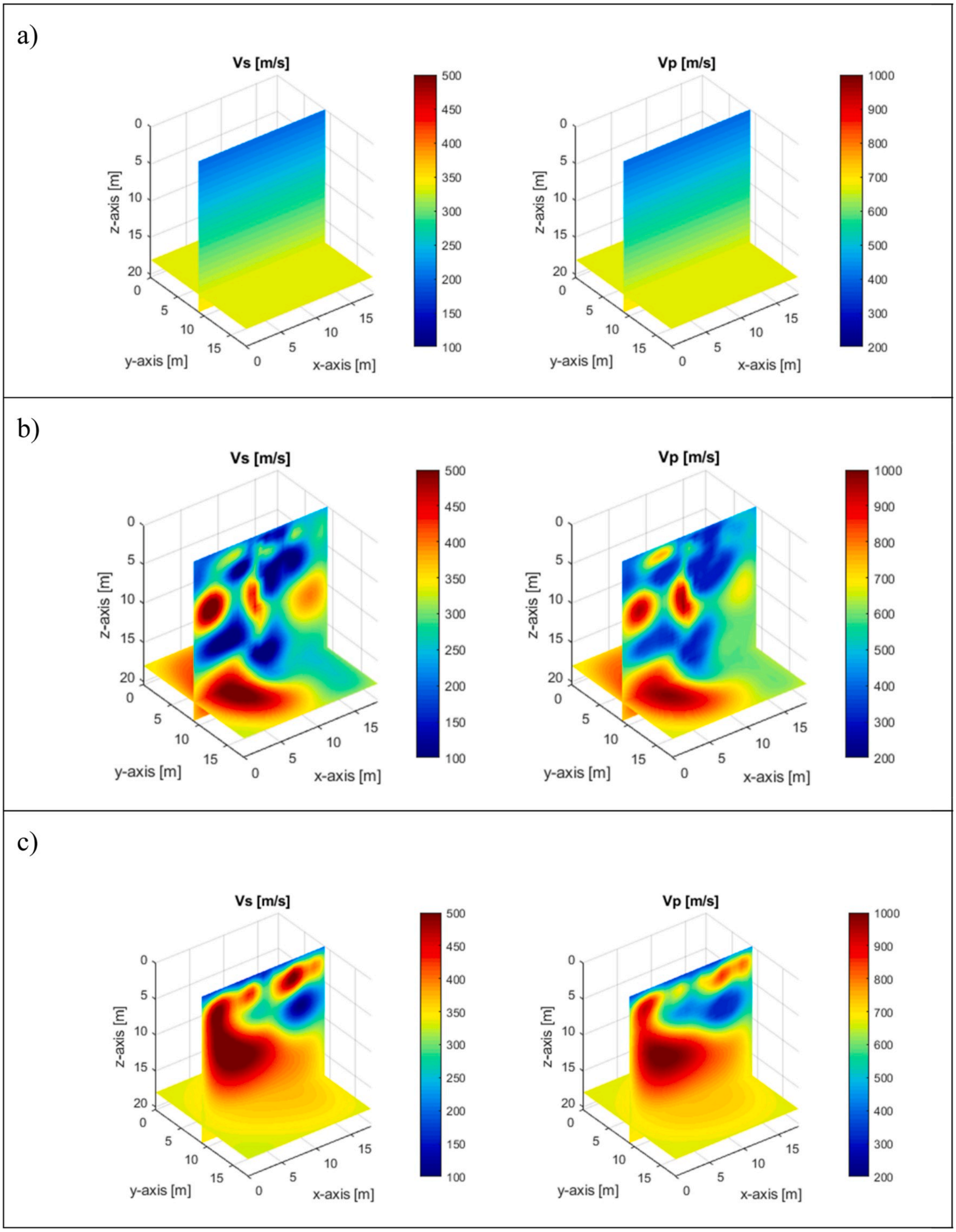

Fig. 8. Field experiment: distribution of Vs and Vp for the initial model (a), the inverted result for SPT source data (b), and the inverted result for surface-based data (c).

noted that waveforms are not very sensitive to the mass density, which does not need to be exactly determined for the inversion analysis.

4.1. SPT-source data analyses

Similar to the synthetic experiment, a medium of 20.4 × 18 × 18 m (depth × length × width) with a grid spacing of 0.6 × 0.75 × 0.75 m (depth × length × width) was used for the analyses (Fig. 6a). The source locations (actual depths of SPT spoon) were rounded to the nearest grid points based on the vertical grid spacing of 0.6 m used in the numerical analyses. The measured field data of the SPT source were filtered through two frequency bandpasses: 10–30 Hz and 10–40 Hz, and used in separate 100 iteration inversions.

To account for attenuation damping of the field data, the estimated data generated from the elastic forward solver were adjusted by an offset dependent correction factor in the form of $y(r) = Ar^{\alpha}$, where r is the source-receiver distance. Parameters A and α were determined through an iterative inversion process to minimize the energy of the waveform

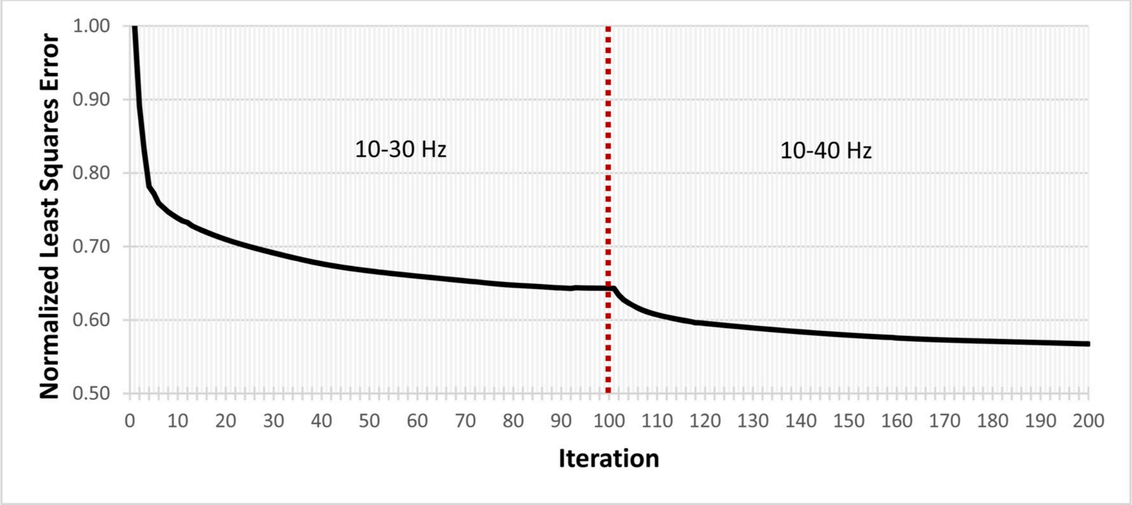

Fig. 9. Field experiment: normalized least squares error for SPT source data.

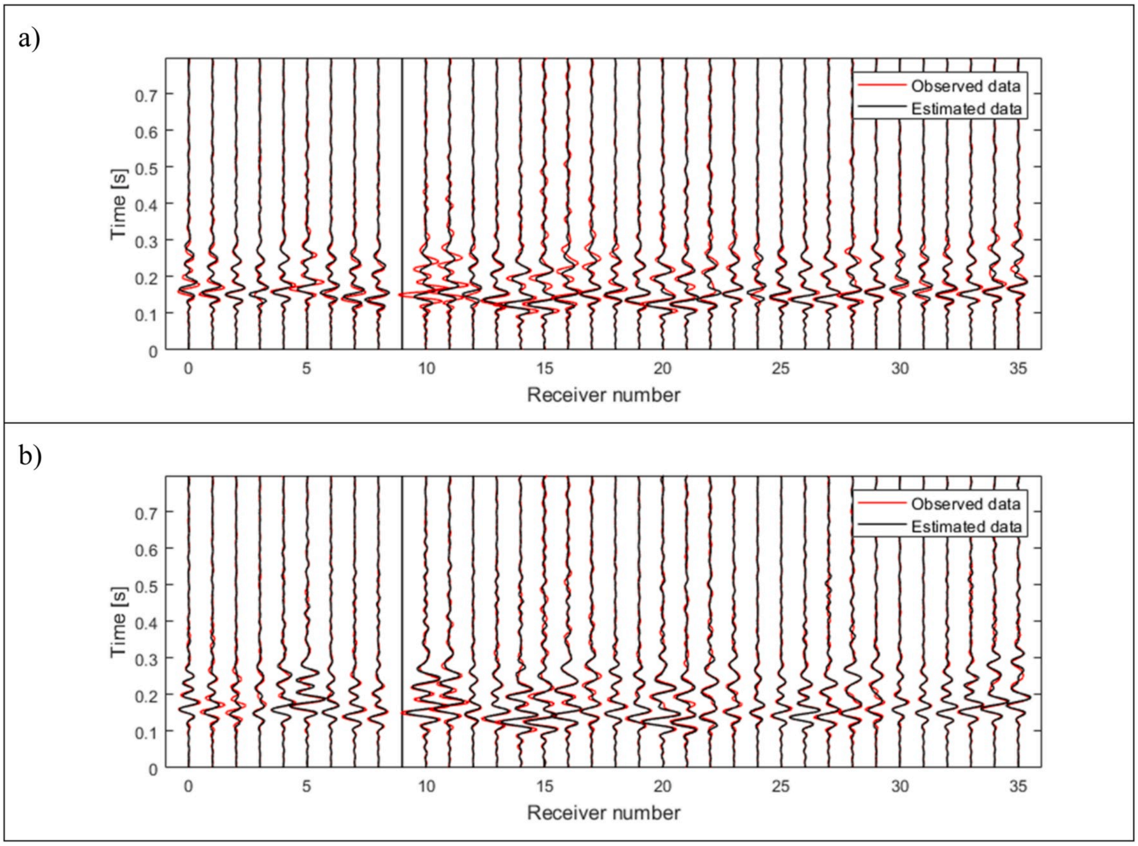

Fig. 10. Field experiment: waveform comparison between the observed data from the SPT-source and estimated data for a sample shot associated with a) the initial model and b) the final inverted result at iteration 200. Channel 9 with poor data is removed from analysis.

residuals. These parameters were determined at the beginning of each inversion run and kept constant for each run. The correction factor y(r) is mostly accounted for material damping. The geometrical damping of the wavefield is already accounted for in the 3D forward simulation.

The first inversion started with the initial model (Fig. 8a), using the filtered data of 10–30 Hz. The second inversion continued with the result of the first inversion as the input velocity model, using the filtered data of 10–40 Hz. Both inversions ran for the preset number of 100 iterations. The error reduced continuously from a normalized value of 1.0 at the start of the inversion process to 0.63 at the end of the first inversion stage (100 iterations), to a value of 0.58 at the end of the second stage at 200 iterations (Fig. 9). Unlike the synthetic analysis, no spike in the normalized error at the transition of the two frequency stages was observed. This means that less wave energy from 30 to 40 Hz was added to the wavefield with the increase of frequency. In addition, most subsurface features had already been revealed by the first frequency stage, and the velocity model was more in agreement with the higher frequency results.

Shown in Fig. 10 is the waveform comparison between the observed (measured) data from a sample SPT-source and estimated data

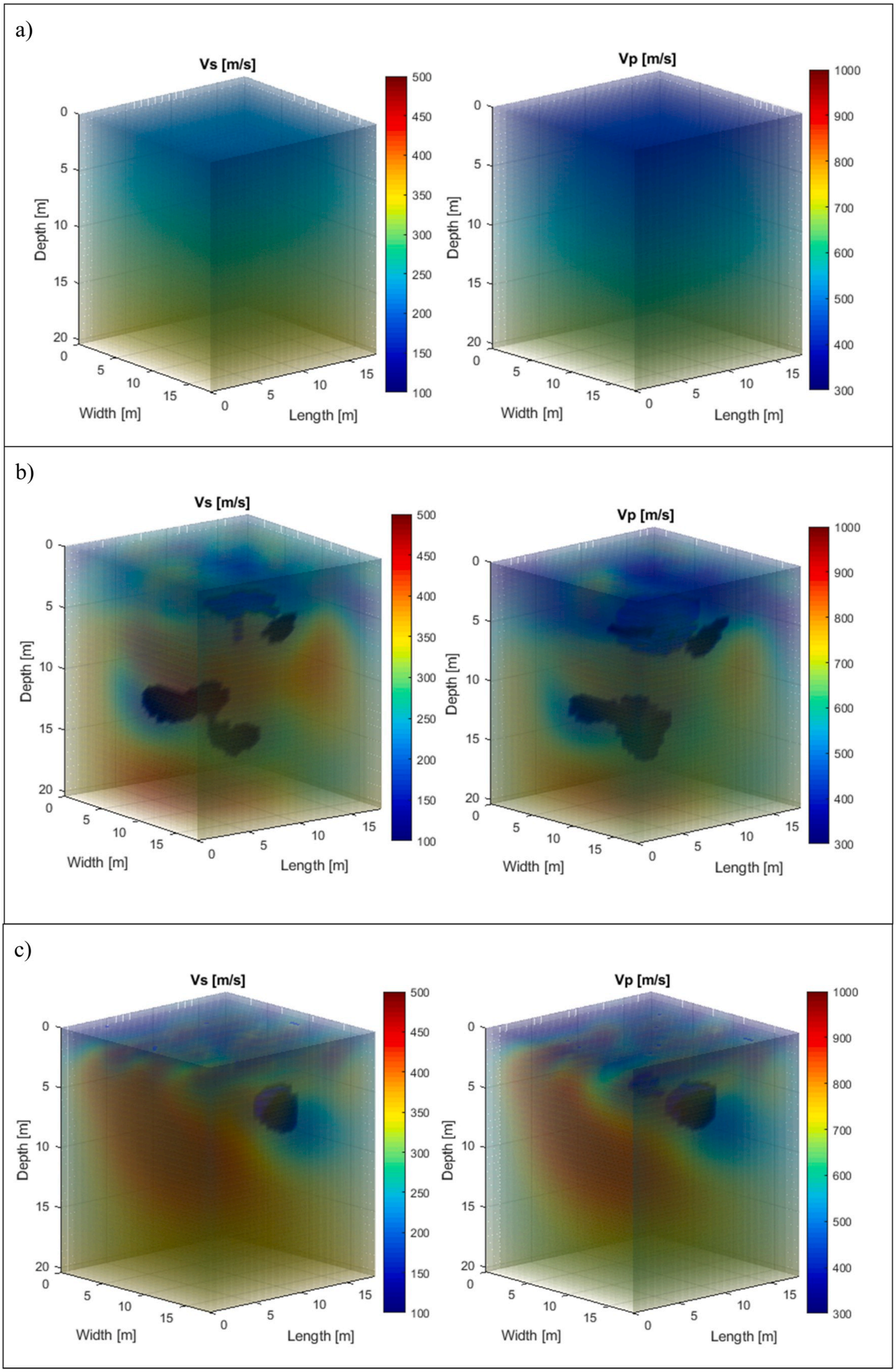

Fig. 11. Field experiment: 3D rendering of the Vs (left) and Vp (right) in m/s for the initial model (a), the final inverted result of the SPT-source data (b) and the final inverted result of the surface-based data (c).

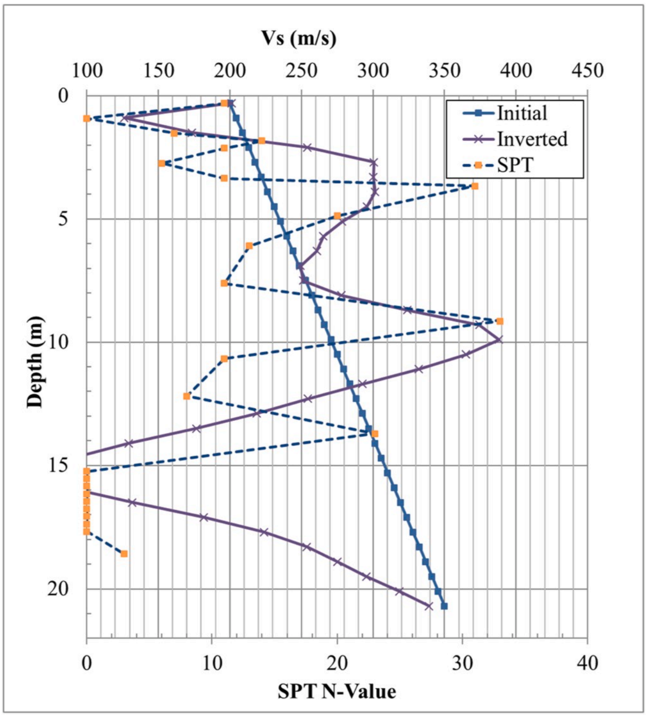

Fig. 12. Comparison of the velocity variation with the SPT N-values for the final inverted result of the SPT-source seismic data and the initial velocity.

associated with the initial model (Fig. 10a) and the final inverted result (Fig. 10b). As seen in the observed data, the seismic waveforms from an embedded SPT blow are present in all of the ground surface geophones, exhibiting both consistent wave propagation pattern and magnitude. During inversion, the waveform match improved for most of the channels. No cycle skipping or matching of the wrong peaks is seen, suggesting the sufficiency of the initial model.

Shown in Fig. 8b is the final inverted result for the SPT-source data. Vs profile (Fig. 8b, left) consists of a soft layer from the ground surface to about 7 m depth with shallow low-velocity anomalies, underlain by a stiff layer. Based on SPT samples, the soft and stiff layers are soil and weathered limestone, respectively. Interestingly, there exist two connected voids with very low Vs (40–100 m/s) inside the limestone layer, at 14–18 m depth. One of them lies outside of the SPT boring and was not observed from the drilling log. The Vp profile (Fig. 8b, right) is consistent with Vs profile, including soil/limestone layers and low-velocity anomalies/voids.

4.2. *Surface-based data analyses*

The surface-based data (surface source and receiver) was inverted using the same initial model as that of the in-depth source data (Fig. 8a). The same frequency bandpasses of 10–30 Hz and 10–40 Hz with the same number of iterations were also used during the surface-based inversion analysis. The final inverted results of the surface-based data (Fig. 8c) reveal one shallow low-velocity zone at the right of the medium, and a high-velocity zone at the left of the medium. As expected, the deep voids inside the limestone layer cannot be identified from the surface-based data. Again, this is due to the limited test area on the surface (18 × 18 m) as well as large reflection of surface source energy at the soil/limestone boundary.

For better viewing of subsurface features, Fig. 11 shows the 3D renderings of Vs and Vp of the initial model, and inverted results of the SPT-source and surface-based data. Again, the two deep voids (14–18 m depth) are clearly shown in the result of the SPT-source data (Fig. 11b, left), but not in the result of the surface-based data (Fig. 11c). The Vp renderings are similar to the Vs renderings, except the two deep voids are merged into a larger void (Fig. 11b, right).

Shown in Fig. 12 is the comparison of the initial Vs, the inverted Vs (iteration 200) and the SPT N-values along the vertical source line (borehole) at the center of the medium. The initial and inverted Vs values were sampled at each grid point along the depth. A good overall match of the SPT N-values and the inverted Vs profile is observed, including identification of low-velocity zones at about 1 m and 15 m depths and high-velocity zones at about 4 m and 9 m depths. The inverted Vs profile is not as erratic as the SPT N-values. This is due to the regularization used in inversion, which partially ties adjacent cells and smooths velocity models. Reducing the regularization level (e.g. using smaller λ_1 and λ_2 values, Eq. (6)) can increase the model contrast and improve the match with SPT N-values. However, it leads to less optimization stability and produces more inversion artifacts.

In summary, based on the field experiment result, the presented SPT-seismic method shows the excellent capability for deep site characterization. It should be used whenever an SPT is used, particularly for cases of limited area on the ground surface (not good for surface-based testing), subsurface conditions with a large stiffness contrast (soil/rock), or thick rock mass. In such cases, the depth of investigation from traditional surface-based seismic methods is often limited near the top of rock mass due to poor signal coverage in rock. Thus, the SPT-seismic method is strongly recommended for these cases to obtain necessary characterized resolution and accuracy with depths.

5. Conclusion

This paper presents a new geophysical investigation approach, SPT-seismic testing for deep site characterization. Seismic energy and waveform data generated from a SPT hammer advancing a spoon sampler in a borehole at depth is recorded with a 2D grid of geophones on the ground surface. The recorded data is then analyzed by a 3D full-waveform inversion (3D FWI) to obtain detailed 3D subsurface structure of soil and rock outside the borehole. The main advantages of this approach are: 1) the in-depth source waveform data can be acquired without the requirement of separate geophysical boreholes, 2) unlike surface-source data dominated by surface waves, the in-depth source data is rich in body waves, which allow higher characterized resolution with depth and, 3) traditional testing within SPT borehole (N-values, tube sampling, coring, etc.) are also available.

Both full-scale synthetic and field experiments were carried out to assess the viability of the approach. In the synthetic experiment, the 3D FWI analysis with in-depth sources and surface receivers successfully recovered a subsurface profile with variable layers along with a deeply buried void. In the case of field testing, the analysis was able to identify the 3D S-wave and P-wave velocities within a 9 m zone around the SPT boring, which included identification of two deep voids at 14–18 m depth within karst limestone. In addition, the inverted S-wave velocities of soil and rock were in general agreement with recorded SPT N-values. It is concluded that the SPT-seismic testing is an economical and efficient tool for obtaining properties of soil and rock both within the borehole as well outside (i.e. 3D volume) for site characterization in the design and construction of deep foundations.

Declaration of competing interest

The authors declare that they have no known competing financial interests or personal relationships that could have appeared to influence the work reported in this paper.

CRediT authorship contribution statement

Majid Mirzanejad: Writing - original draft, Methodology, Formal analysis. **Khiem T. Tran:** Writing - review & editing, Conceptualization, Data curation, Investigation, Methodology, Funding acquisition.

Michael McVay: Writing - review & editing, Conceptualization, Data curation, Investigation, Methodology, Funding acquisition. **David Horhota:** Writing - review & editing, Project administration, Supervision, Validation. **Scott J. Wasman:** Writing - review & editing, Data curation, Validation.

Acknowledgments

This study was supported by the National Science Foundation: grants CMMI-1637557, CMMI 1850696, and the Florida Department of Transportation (FDOT): grant BDV31-977-82. We thank the FDOT for assisting to conduct the SPT-seismic data.

Appendix A. Supplementary data

Supplementary data to this article can be found online at https://doi.org/10.1016/j.soildyn.2020.106196.

References

[1] Nguyen TD, Tran KT. Site characterization with 3D elastic full-waveform tomography. Geophysics 2018;83(5):R389–400. https://doi.org/10.1190/geo2017-0571.1.

[2] Tran KT, Mirzanejad M, McVay M, Horhota D. 3-D time-domain Gauss–Newton full waveform inversion for near-surface site characterization. Geophys J Int 2019;217(1):206–18. https://doi.org/10.1093/gji/ggz020.

[3] Mirzanejad M, Tran KT. 3D viscoelastic full waveform inversion of seismic waves for geotechnical site investigation. Soil Dynam Earthq Eng 2019;122:67–78. https://doi.org/10.1016/j.soildyn.2019.04.005.

[4] Fehler M, Pearson C. Cross-hole seismic surveys: applications for studying subsurface fracture systems at a hot dry rock geothermal site. Geophysics 1984;49(1):37–45. https://doi.org/10.1190/1.1441559.

[5] Cao S, Greenhalgh S. Cross-well seismic tomographic delineation of mineralization in a hard-rock environment. Geophys Prospect 1997;45(3):449–60. https://doi.org/10.1046/j.1365-2478.1997.370280.x.

[6] Bregman ND, Bailey RC, Chapman CH. Crosshole seismic tomography. Geophysics 1989;54(2):200–15. https://doi.org/10.1190/1.1442644.

[7] Ivansson SVEN. Seismic borehole tomography—theory and computational methods. Proc IEEE 1986;74(2):328–38. https://doi.org/10.1109/PROC.1986.13459.

[8] Wong J, Bregman N, West G, Hurley P. Cross-hole seismic scanning and tomography. Lead Edge 1987;6(1):36–41. https://doi.org/10.1190/1.1439327.

[9] Pratt RG, Goulty NR. Combining wave-equation imaging with traveltime tomography to form high-resolution images from crosshole data. Geophysics 1991;56(2):208–24. https://doi.org/10.1190/1.1443033.

[10] Pratt RG, Shipp RM. Seismic waveform inversion in the frequency domain, Part 2: fault delineation in sediments using crosshole data. Geophysics 1999;64(3):902–14. https://doi.org/10.1190/1.1444598.

[11] Zhou B, Greenhalgh SA. Crosshole seismic inversion with normalized full-waveform amplitude data. Geophysics 2003;68(4):1320–30. https://doi.org/10.1190/1.1598125.

[12] Wang Y, Rao Y. Crosshole seismic waveform tomography–I. Strategy for real data application. Geophys J Int 2006;166(3):1224–36. https://doi.org/10.1111/j.1365-246X.2006.03030.x.

[13] Cheng F, Liu J, Wang J, Zong Y, Yu M. Multi-hole seismic modeling in 3-D space and cross-hole seismic tomography analysis for boulder detection. J Appl Geophys 2016;134:246–52. https://doi.org/10.1016/j.jappgeo.2016.09.014.

[14] Rao Y, Wang Y, Chen S, Wang J. Crosshole seismic tomography with cross-firing geometry. Geophysics 2016;81(4):R139–46. https://doi.org/10.1190/geo2015-0677.1.

[15] Butchibabu B, Sandeep N, Sivaram YV, Jha PC, Khan PK. Bridge pier foundation evaluation using cross-hole seismic tomographic imaging. J Appl Geophys 2017;144:104–14. https://doi.org/10.1016/j.jappgeo.2017.07.008.

[16] Ng YCH, Danovan W, Ku T. The potential of seismic cross-hole tomography for geotechnical site investigation. In: E3S web of conferences, 92; 2019. p. 18006. https://doi.org/10.1051/e3sconf/20199218006. EDP Sciences.

[17] Tran KT, Hiltunen DR. Inversion of combined surface and borehole first-arrival time. J Geotech Geoenviron Eng 2011;138(3):272–80. https://doi.org/10.1061/(ASCE)GT.1943-5606.0000587.

[18] Virieux J. P-SV wave propagation in heterogeneous media: velocity-stress finite-difference method. Geophysics 1986;51:889–901. https://doi.org/10.1190/1.1442147.

[19] Robertsson JO. A numerical free-surface condition for elastic/viscoelastic finite-difference modeling in the presence of topography. Geophysics 1996;61(3):1921–34. https://doi.org/10.1190/1.1826736.

[20] Komatitsch D, Martin R. An unsplit convolutional perfectly matched layer improved at grazing incidence for the seismic wave equation. Geophysics 2007;72(5):SM155–67. https://doi.org/10.1190/1.2757586.